Intra- and intersite electronic excitations in multiferroic TbMnO₃ probed by resonant inelastic x-ray scattering

J. M. Chen,[1,][*] J. M. Lee,[1,2] S. W. Huang,[1,2] K. T. Lu,[1] H. T. Jeng,[3] C. K. Chen,[1] S. C. Haw,[1] T. L. Chou,[1] S. A. Chen,[1]
N. Hiraoka,[1] H. Ishii,[1] K. D. Tsuei,[1] and T. J. Yang[2]

[1]*National Synchrotron Radiation Research Center (NSRRC), Hsinchu 30076, Taiwan, Republic of China*
[2]*Department of Electrophysics, National Chiao Tung University, Hsinchu 30010 Taiwan, Republic of China*
[3]*Institute of Physics, Academia Sinica, Taipei 11529 Taiwan, Republic of China*
(Received 19 May 2010; revised manuscript received 4 July 2010; published 27 September 2010)

Mn $3d$ valence states and elementary electronic excitations in single-crystalline TbMnO₃ were probed with resonant inelastic x-ray scattering (RIXS) (or resonant x-ray emission spectroscopy, RXES), polarized x-ray absorption spectra and *ab initio* electron-structure calculations. Polarized Mn K-edge x-ray absorption spectra of TbMnO₃ crystals exhibit a significant anisotropy along three crystallographic directions, particularly for the white-line region. The $1s3p$-RXES spectra obtained at the Mn K edge reveal that the quadrupolar Raman regime is restricted predominantly to below the pre-edge peak whereas the fluorescence regime starts from the first pre-edge peak of $1s \rightarrow 3d$ transitions, indicating a relatively delocalized character of unoccupied Mn $3d$ states. The additional Kβ emission profile at energy loss ~ 62 eV is attributed to the off-site dipole Mn $1s$-Mn′ $3d$ and/or Mn $1s$-Tb $5d$ transitions, originating from hybridization between Mn $4p$ states and neighboring Mn′ $3d$/Tb $5d$ states. The off-site dipole transition makes a considerable contribution to the pre-edge region of Mn K-edge spectrum. Three prominent RIXS features at ~ 2.9, 7, and 11 eV were observed. Based on GGA+U calculations, the 7 eV region corresponds to transitions from O $2p$ states to unoccupied minority Mn $3d$ states, whereas the 11 eV band is ascribed to transitions from the O $2p$ band to the empty Tb $5d$ band. The broad 2.9 eV band is attributed to the coexistence of on-site Mn $3d$-Mn $3d$ and off-site Mn $3d$-Mn′ $3d$ transitions.

I. INTRODUCTION

As a consequence of a competition and interplay between charge, spin, orbital and lattice degrees of freedom under a strong electron correlation, perovskite manganites RMnO₃ (R=rare-earth ion) exhibit varied and fascinating physical phenomena, such as charge and orbital ordering,[1–3] metal-insulator transitions,[4] colossal magnetoresistance,[5–9] half-metallic behavior,[10,11] and multiferroicity.[12–19] In particular, magnetoelectric (ME) multiferroics, which display simultaneously ferroelectric and magnetic long-range order with cross coupling, have attracted renewed attention because of both their intrinsic scientific interest and relevant prospective applications in devices with novel functions. The ME effect in a material signifies an electric polarization generated with a magnetic field or a magnetization induced with an electric field. Of all known multiferroic materials, RMnO₃ rare-earth manganites, such as TbMnO₃ and DyMnO₃, attract particular interest.[12–14,18,20]

TbMnO₃ (space group *Pbmn*) exhibits an orthorhombically distorted perovskite structure near 300 K, and an incommensurate lattice modulation at the Néel temperature (T_N=42 K) forming a collinear sinusoidal antiferromagnetic (AF) ordering of Mn spins oriented along the [010] direction. Below T=28 K, the magnetic structure of Mn spins becomes a noncollinear spin arrangement forming a cycloid in the *b*-*c* plane and an electric polarization simultaneously appears along the *c* axis.[12,20] The ME phase diagram of TbMnO₃ varies significantly along the three crystallographic axes parallel to which a magnetic field is applied.[20]

According to the Goodenough-Kanamori rule, a virtual *d-d* orbital excitation between overlapping orbitals from neighboring transition-metal (TM) sites with each half-filled *d* orbital brings about antiferromagnetic superexchange interactions, whereas a virtual *d-d* orbital excitation between two orthogonal orbitals from neighboring transition-metal sites is from a half-filled *d* orbital to an empty *d* orbital, leading to ferromagnetic superexchange interactions.[21,22] This superexchange interaction is responsible for magnetism in diverse materials including transition-metal oxides[23] and strongly correlated electronic systems.[24] Recent theoretical calculations in undoped manganites reveal that a magnetically incommensurate phase of RMnO₃ (R=rare earth) might arise from a competition between the Mn $3d$ antiferromagnetic superexchange interaction and the Mn $3d$ ferromagnetic superexchange interaction.[25–27] The effective superexchange interactions between the Mn $3d$ states at separate Mn sites therefore play a crucial role in the multiferroic behavior of RMnO₃. The superexchange interactions between the Mn $3d$ states at separate sites in RMnO₃ are strongly associated with hybridization of Mn $3d$ orbitals with neighboring orbitals such as O $2p$ states and Mn $4p$ orbitals.[28,29]

In 3d TM oxides, the small pre-edge features of TM K-edge absorption spectra are generally explained in terms of quadrupole $1s$-$3d$ transitions or modifications of the dipole transition probability due to hybridization between TM $4p$ and neighboring TM′ $3d$ states. For manganites, the latter are assumed to be dominant but there has been no direct evidence to support this hypothesis.[30] According to an experimental point of view, the intersite Mn $4p$-Mn′ $3d$ mixing mediated by intervening O $2p$ orbitals is expected to be correlated with the delocalized character of unoccupied Mn $3d$ states in RMnO₃ because Mn $4p$ states have a large radial
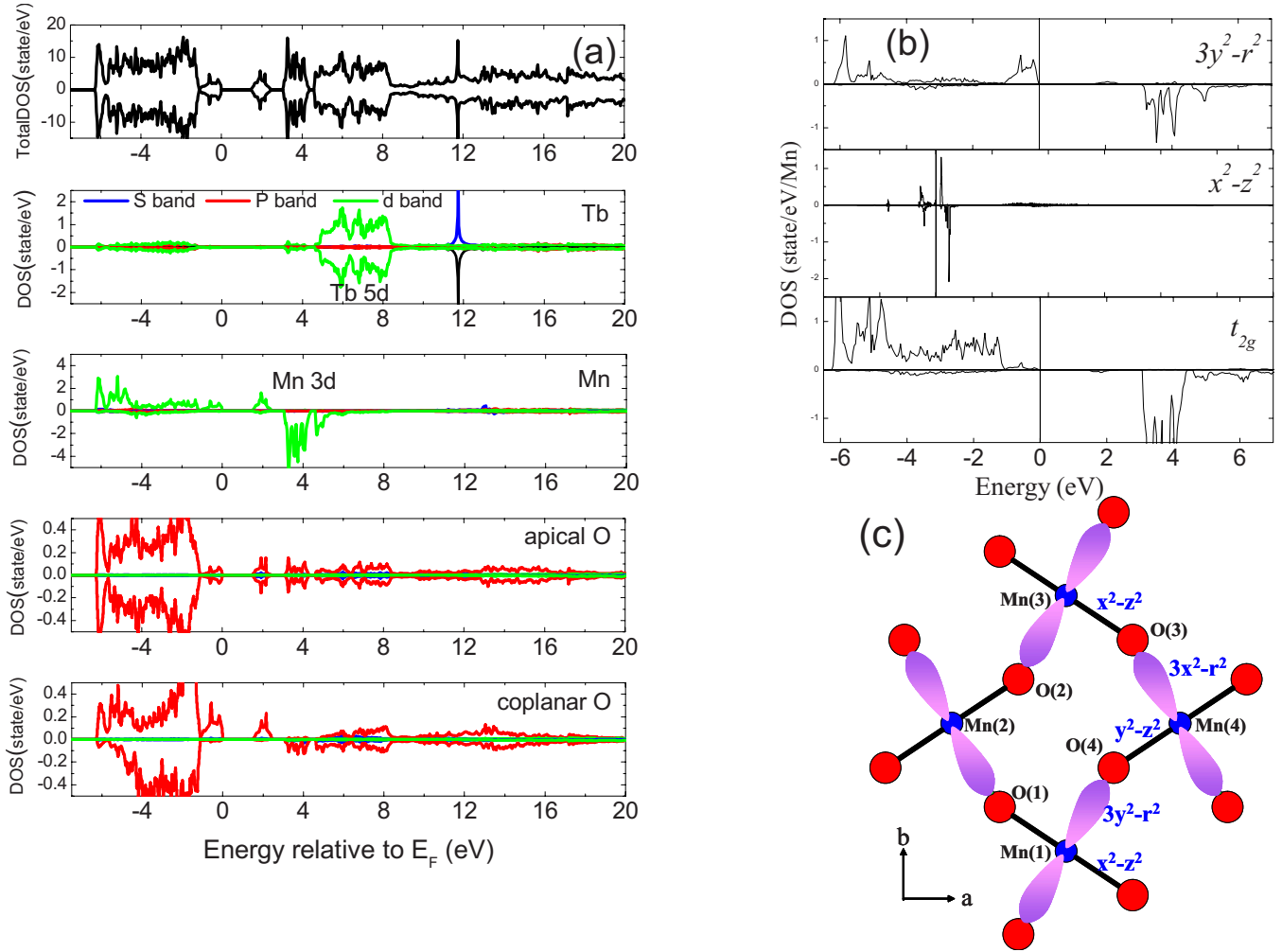
FIG. 1. (Color online) (a) Total and site-decomposed densities of states and (b) partial densities of states of Mn projected onto fivefold $3d$ orbitals for an A-type anti-ferromagnetic structure of TbMnO$_3$ calculated with the GGA+U method. For each panel the upper half denotes the majority and the lower half the minority spin states. The energy zero is at the Fermi level. (c) Schematic of the crystal structure of TbMnO$_3$ with orbital (lobes) ordering within the ab plane.

extent. However, definitive experimental evidence of neither delocalization of unoccupied Mn $3d$ states nor intersite hybridization of Mn $4p$ orbitals with neighboring Mn′ $3d$ states in manganites has been provided.[31]

The order of excitation energies, such as intersite d-d excitation between neighboring transition-metal sites and onsite Coulomb repulsion (U) is several electron volts. Oxygen-mediated intersite d-d interactions between neighboring metal sites have a crucial impact on transport, magnetic, and electronic properties of strongly correlated electron materials.[32,33] A comprehensive understanding of elementary orbital excitations, in particular, intersite d-d excitations, is essential to understand the physics of strongly correlated systems, such as manganites. Although numerous reports of the structural, magnetic, and dielectric properties of RMnO$_3$ (R=Tb and Dy) have appeared,[14,20,34–36] a detailed study of the low-energy excited states of this system remains lacking. With the advantage of momentum resolution and bulk sensitivity, resonant inelastic x-ray scattering (RIXS) spectra (or resonant x-ray emission spectroscopy, RXES) in the hard x-ray regime have emerged as a promis-

ing tool to investigate the elementary electronic excitation of various materials, in which a core electron is excited resonantly by an incident x-ray photon and this core excited state decays radiatively on emitting an x-ray photon.[37–41] The RIXS (or RXES) is thus a second-order optical process for which d-d transitions are allowed although dipole forbidden for a first-order optical process. The RIXS (or RXES) spectra were previously shown to provide detailed information about the bulk electronic properties of various materials, such as the degree of localization, electronic occupancy, and the off-site d-d excitation between separate transition-metal sites.[31,39,42] In this work, we recorded lifetime-broadening-suppressed x-ray absorption spectra and resonant inelastic x-ray scattering (or resonant x-ray emission spectra) at the Mn K edge coupled with *ab initio* electron structure calculations to investigate the intra- and intersite electronic excitations for multiferroic TbMnO$_3$ crystals.

II. EXPERIMENTAL

Untwinned orthorhombic TbMnO$_3$ single crystals were grown by the high-temperature solution method with a PbF$_2$

flux in a Pt crucible. The rocking curve of the TbMnO$_3$ crystal has full width $\sim 0.01°$ at half maximum (FWHM) for the (0 0 2) Bragg reflection, indicating the crystal quality to be excellent. Two crystal surfaces with crystallographic directions (100), (010) (i.e., *ab* plane) and (100), (001) (i.e., *ac* plane) were aligned with an x-ray diffractometer.

The RIXS measurements were performed at the Taiwan beamline BL12XU at SPring-8 in Japan. Incident x-rays from a SPring-8 standard undulator were monochromatized with a Si(111) double-crystal monochromator. The emitted x-ray fluorescence was analyzed with a Si(440) spherically bent analyzer of a 1 m Rowland-circle spectrometer arranged on a horizontal plane. The incident energy was calibrated with the known Mn metal *K*-edge absorption inflection point at 6539 eV. For energy calibration of the RIXS spectra the elastic peak positions and the monochromator calibration were related. The overall resolution was estimated to be ~ 0.9 eV from the full FWHM of the elastic peak measured at the Mn $K\beta_{13}$ emission energy, ~ 6492 eV. Typical inelastic count rates were between 1 and 10 counts s^{-1}. The background, as measured on the energy gain side, was ~ 0.1 counts s^{-1}. All data were recorded at room temperature. Separate TbMnO$_3$ crystals with the same axis showed great reproducibility of the experimental Mn *K*-edge absorption spectra, indicating the high quality of our crystals.

III. RESULTS AND DISCUSSION

We calculated the electronic structure from first principles to obtain the band structure of TbMnO$_3$. To include the effects of strong Coulomb interactions among 3*d* electrons in TbMnO$_3$, we used the generalized-gradient approximation plus an on-site Coulomb interaction *U* (GGA+*U*) scheme based on density-functional theory and the full-potential projected augmented-wave method as implemented in the Vienna *ab initio* simulation package (VASP).[43,44] In these calculations, we used an effective on-site Coulomb energy parameter $U = 5$ eV and exchange parameter $J = 0.87$ eV for Mn 3*d* electrons.

Figure 1(a) shows the total and site-decomposed densities of states for the *A*-type AF structure of TbMnO$_3$ from our calculations. The plotted range of energy is from -7 to 20 eV; the Fermi level is set to zero. The bands in a broad series between -2 and -7 eV in TbMnO$_3$ arise from O 2*p* orbitals. Above these O 2*p* bands, and separated from them by an energy gap, are the Mn 3*d* bands. Tb 5*d* states hybridized with O 2*p* states are located in a band spanning energy range 5–10 eV above the Fermi level. A broad band between 10 and 15 eV corresponds to the high-lying unoccupied Mn 4*sp* and Tb 6*s* states hybridized with O 2*p* states. As noted from Fig. 1(a), hybridization between O 2*p* and the Mn 3*d* (or 4*p*) bands is clearly observed.

Figure 1(b) displays the partial density of states of Mn projected onto the fivefold 3*d* orbitals. The Mn 3*d* bands are divided into two subbands—the lower energy t_{2g} (d_{xy}, d_{yz}, and d_{xz}) bands, and the higher energy e_g bands—as a result of crystal-field splitting by octahedral oxygen anions in TbMnO$_3$. Through a strong Jahn-Teller (JT) effect, the $e_g\uparrow$ band splits into two subbands $e_g^1\uparrow$ and $e_g^2\uparrow$ in TbMnO$_3$. There
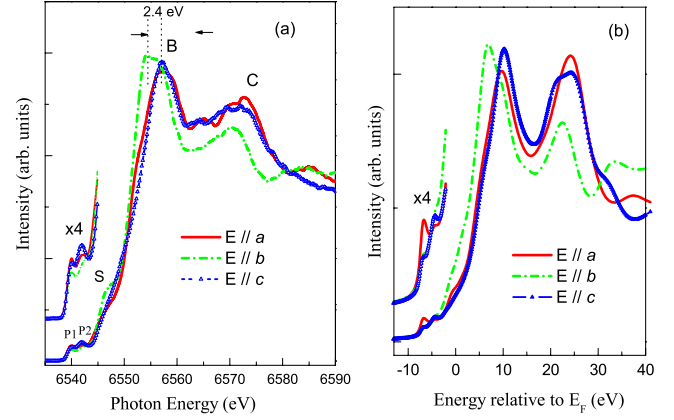

FIG. 2. (Color online) (a) Polarization-dependent Mn *K*-edge x-ray absorption spectra of single-crystalline TbMnO$_3$ for polarizations $E\|a$, $E\|b$, and $E\|c$ measured in the partial-fluorescence-yield mode at room temperature with enlarged pre-edge region. (b) Simulated polarized Mn *K*-edge spectra of TbMnO$_3$ with enlarged pre-edge region using the FDMNES code.

is a small indirect gap between the JT-split Mn $e_g^1\uparrow$ and $e_g^2\uparrow$ bands. Based on GGA+*U* calculations, the occupied $e_g^1\uparrow$ and unoccupied $e_g^2\uparrow$ bands are dominated by $d_{3x^2-r^2}$ and $d_{y^2-z^2}$ orbitals, respectively, in one coplanar Mn ion, whereas they exhibit predominantly $d_{3y^2-r^2}$ and $d_{x^2-z^2}$ character, respectively, for the other coplanar Mn ion, as represented in Fig. 1(c). TbMnO$_3$ hence exhibits a staggered $d_{3x^2-r^2}/d_{3y^2-r^2}$-type orbital ordering in the *ab* plane, similar to that of YMnO$_3$ and LaMnO$_3$.[45,46] The half-filled $e_g^1\uparrow$ orbitals of Mn^{3+} ions occupy the long Mn-O2(*l*) site projected predominantly along the *b* axis, whereas unoccupied $e_g^2\uparrow$ orbitals locate at the short Mn-O2(*s*) site projected predominantly along the *a* axis. As for the spin-down channel, one $e_g\downarrow$ band ($d_{3z^2-r^2}$) is mixed with the $t_{2g}\downarrow$ bands at 3–4 eV above the Fermi level, whereas the other $e_g\downarrow$ band ($d_{x^2-y^2}$) is located ~ 4.5 eV above the Fermi level [Fig. 1(b)].

Figure 2(a) shows polarized Mn *K*-edge high-resolution x-ray absorption spectra of TbMnO$_3$ crystals for polarizations $E\|a$, $E\|b$, and $E\|c$. The absorption spectra were recorded in the partial fluorescence yield with the spectrometer set to the peak of the Mn $K\beta_{1,3}$ fluorescence line and varying the incident energy. The Mn *K*-edge x-ray absorption spectra comprise two pre-edge peaks (labeled P1 and P2), a shoulder (labeled S), and an intense white line on the side of greater photon energy (peak B). The pre-edge features (P1 and P2) are generally ascribed to quadrupole 1*s*-3*d* or modifications of the dipole transition probability due to hybridization between 3*d* and 4*p* states. As shown in Fig. 1(a), Tb 5*d* states are located in energy range 5–10 eV above the Fermi level. Feature S is attributed to the hybridization between the Mn 4*p* states and Tb 5*d* orbitals. The white line (peak B) is related to 1*s* to 4*p* transitions. Feature C gains intensity from the multiple scattering contribution of MnO$_6$ surrounded by eight Tb. As shown in Fig. 2(a), Mn *K*-edge x-ray absorption spectra exhibit a significant anisotropy along three crystallographic directions, particularly for the white line region (peak B). A significant energy shift to smaller energy ~ 2.4 eV is observed for the maximum of the white line of
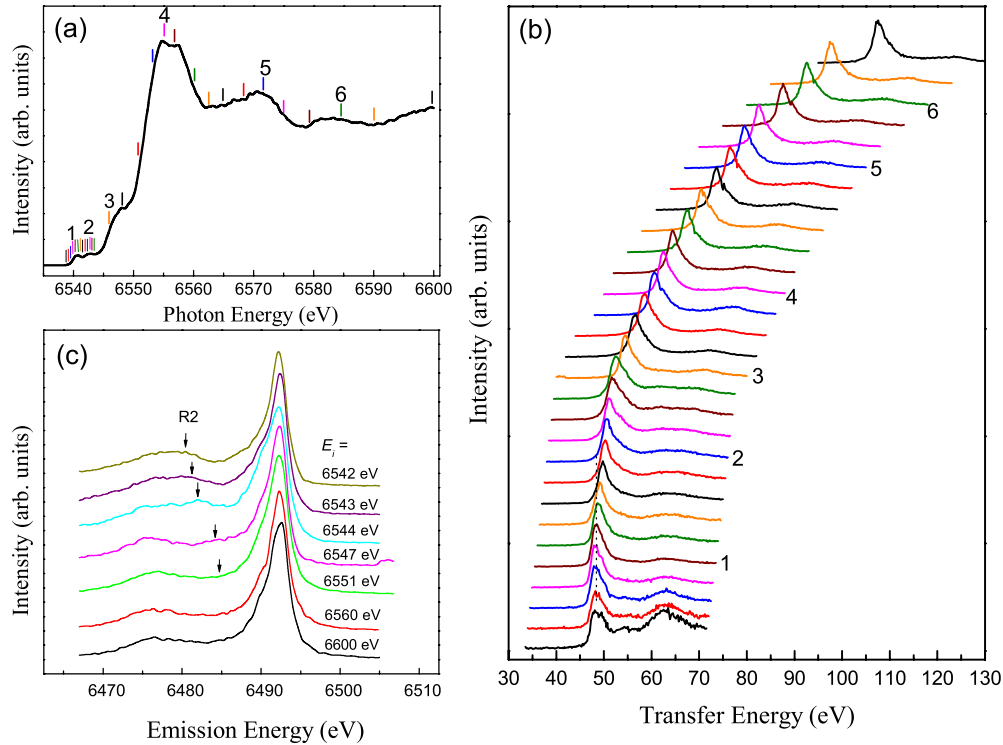
FIG. 3. (Color online) (a) Polarized Mn K-edge x-ray absorption spectra of TbMnO$_3$ crystals for $E\|b$ polarization at room temperature. Ticks in the Mn K-edge absorption spectrum indicate the excitation energies at which the resonant x-ray emission spectra were recorded. (b) $1s3p$-resonant x-ray emission spectra of single-crystalline TbMnO$_3$ measured at room temperature as a function of transfer energy for $E\|b$ polarization. The resonant x-ray emission spectra are plotted from bottom to top in increasing incident photon energy. The number indicated in the emission spectra corresponds to the excitation energy marked in the Mn K-edge x-ray absorption spectra. Each spectrum is normalized using its maximum value. (c) Mn $K\beta$ emission spectra at incident energies of E_i=6542–6600 eV. New Raman feature R2 is observed at energy loss $\sim$62 eV. Each spectrum is normalized using its maximum value.

the Mn K-edge spectrum obtained along $E\|b$ relative to $E\|a$ and E$\|c$. This condition implies strong anisotropic Mn-O bonding within the ab plane in TbMnO$_3$ and weak covalency along the b axis. The origin of this energy difference is attributed to a Jahn-Teller distortion and orbital ordering of MnO$_6$ octahedra in TbMnO$_3$.

As shown in Fig. 1(c), the strong Jahn-Teller distortion leads to a shorter distance between O2 and O4, which in turn slightly changes the next-nearest-neighbor (NNN) antiferromagnetic (AFM) superexchange interaction through the Mn(1)-O4-O2-Mn(3) paths. This distortion also suppresses strongly the predominant nearest-neighbor (NN) ferromagnetic (FM) superexchange interaction ($\sim$$-13$ meV for LaMnO$_3$ and $\sim$$-3$ meV for TbMnO$_3$).[26,47] Under the staggered $d_{3x^2-r^2}$/$3d_{3y^2-r^2}$–type of orbital ordering as shown in Fig. 1(c), the AFM NNN superexchange interaction between Mn(1) and Mn(3) (along the b axis) is stronger than that between Mn(2) and Mn(4) (along the a axis). Thus, a delicate balance of the competition between the NN FM and the NNN AFM superexchange interactions along the b axis leads to a frustrated spin system and gives rise to a noncollinear spiral spin arrangement at low temperatures.[26,48]

We performed polarized Mn K-edge x-ray absorption spectroscopy (XAS) calculations of TbMnO$_3$ using the FD-MNES code.[49] In the present XAS simulation, a self-consistent spherical muffin-tin (MT) full-multiple-scattering (FMS) approach with the real Hedin-Lundqvist exchange-

correlation potential was applied with a cluster radius R =6 Å that corresponds to 75 atoms. The FMS calculations were performed using the MT potential constructed from 10% overlapped MT spheres of the specified radii. Figure 2(b) shows simulated polarized Mn K-edge x-ray absorption spectra of TbMnO$_3$. As noted, the energy of the white line for $E\|b$ polarization is shifted to lower energy relative to polarizations $E\|a$ and $E\|c$. The experimental and calculated Mn K-edge spectra agree satisfactorily.

As noted, the white line region between experimental and calculated Mn K-edge spectra agrees satisfactorily. In contrast, the pre-edge region, particularly for P1 feature, between experimental and calculated Mn K-edge spectra shows a noteworthy discrepancy. The theoretical results based on FDMNES calculations predominantly yield the quadrupole $1s$ $\rightarrow 3d$ transitions, as well as the dipole $1s \rightarrow 4p$ transitions into the $3d$-band region (i.e., so-called dipolar assisted transitions). This discrepancy implies that the off-site dipole transition due to hybridization between Mn $4p$ states and Mn $3d$ states of neighboring Mn atoms makes a considerable contribution to the pre-edge region of Mn K-edge spectrum.

The Mn $3d$ valence states of single-crystalline TbMnO$_3$ were probed with resonant x-ray emission spectra. Figure 3(a) shows polarized Mn K-edge x-ray absorption spectra of TbMnO$_3$ crystals for $E\|b$ polarization at room temperature. Ticks in the Mn K-edge x-ray absorption spectrum indicate the excitation energies at which the RXES spectra [Fig. 3(b)]

were recorded. In Fig. 3(b), the $1s3p$-RXES spectra obtained for single-crystalline $TbMnO_3$ at room temperature are shown for $E\|b$ polarization. The RXES spectra are plotted as a function of transfer energy and ordered from bottom to top in increasing incident photon energies. We analyzed the RXES data in terms of quadrupolar transitions to $1s^{-1}3d^{n+1}$ intermediate states or dipolar-assisted transitions to $1s^{-1}3d^n4p^1$ intermediate states, which are primarily assigned to the pre-edge and white-line spectral regions. The final states are reached by decay of a $3p$ electron, leading to the $3p^{-1}3d^{n+1}$ or $3p^{-1}3d^n4p^1$ configuration. Here, we included the off-site dipole Mn $1s$-Mn$'$ $3d$ and Mn $1s$-Tb $5d$ transitions with Mn$(1s^{-1}3d^n4p)$Mn$'(3d^1)$ and Mn$(1s^{-1}3d^n4p)$Tb$(5d^1)$ intermediate states, respectively. The final states for the off-site dipole transitions yield the Mn$(3p^{-1}3d^n4p)$Mn$'(3d^1)$ and Mn$(3p^{-1}3d^n4p)$Tb$(5d^1)$ configurations.

As clearly seen in Fig. 3(b), the features related to transitions to the localized intermediate $1s^13d^{n+1}$ states appear at a constant transfer energy, characteristic of the so-called Raman regime, as indicated by a vertical dashed line.[31,50,51] Fluorescencelike features, corresponding to the delocalized $3p^{-1}3d^n4p^1$ final states, appear at a linearly dispersed transfer energy with the incident energy. Excitation with x-ray energies well above the white line of Mn K-edge absorption spectrum of $TbMnO_3$ yields two major bands at ~6492.5 and ~6476 eV, which are the Mn $K\beta_{1,3}$ and $K\beta'$ fluorescence lines. As the excitation energy is lowered to near absorption edge (~6551 eV), a new Raman feature (with constant energy loss ~62 eV), labeled R2, appears between $K\beta_{1,3}$ and $K\beta'$ lines, as indicated in Fig. 3(c). By lowering the excitation energy to pre-edge region, Raman lines (labeled R1 and R3) are dominant. In order to analyze the contribution from the Raman and fluorescence components, we fit the whole series of $1s3p$-RXES spectra of $TbMnO_3$. For the fluorescence signals, we need to assume a sum of four symmetrical lines, F1 (i.e., $K\beta_{1,3}$), F2, F3, and F4 (i.e., $K\beta'$). For the Raman components, R1 and R3 are dominant in the pre-edge region. In Fig. 4, we display two examples of the curve fit of the Mn $1s3p$ RXES spectra for $E_i=6543.5$ and 6539.5 eV.

Figure 5 shows the incident photon energy dependence of the intensity of the fluorescence components, Mn $K\beta_{1,3}$ and Mn $K\beta'$, and the Raman components, R1, R2 and R3, of Mn $1s3p$-RXES spectra of $TbMnO_3$ crystals. As noted from Figs. 3(b) and 5, the quadrupolar Raman components R1 and R3 are restricted predominantly to below the first pre-edge peak P1. The fluorescence regime starts from the first pre-peak P1 of $1s\rightarrow 3d$ transitions, implying the delocalization of intermediate $1s^13d^{n+1}$ states and thus a relatively delocalized character of unoccupied Mn $3d$ states. As noted, the Raman component R2 is very broad, observed at incident energies from pre-edge region to white line region. This additional $K\beta$ emission profile R2 in Fig. 3(c) is proposed to be attributed to the contribution of the off-site dipole Mn $1s$-Mn$'$ $3d$ and/or Mn $1s$-Tb $5d$ transitions, as a consequence of hybridization between Mn $4p$ states and neighboring Mn$'$ $3d$/Tb $5d$ states. A similar phenomenon was observed for La_2CuO_4 and $Y_{1-x}Pr_xBa_2Cu_3O_7$.[51,52]

Based on the present GGA+U calculations, the Mn $4p$ states are highly delocalized and extend over several Mn
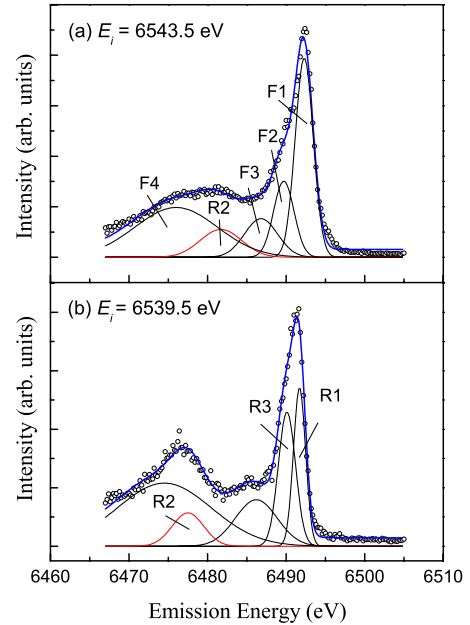

FIG. 4. (Color online) Examples of curve fit for the Mn $1s3p$-RXES spectra obtained for $TbMnO_3$ crystals at incident photon energies of (a) 6543.5 eV and (b) 6539.5 eV. The open circles are the experimental data.

atoms. Besides, Mn $3d$ and Mn $4p$ states are strongly hybridized with O $2p$ states. The off-site Mn $1s$-Mn$'$ $3d$ dipole transition is thus weakly allowed through hybridization of the Mn $4p$ state on the core-excited site (on-site) and the Mn$'$ $3d$ states on neighboring sites (off-site) either directly or via intervening O $2p$ orbitals through Mn $4p$-O $2p$ and O $2p$-Mn $3d$ hybridizations.[53] The pre-edge features P1 and P2 observed in Fig. 2(a) are accounted for with a coexisting
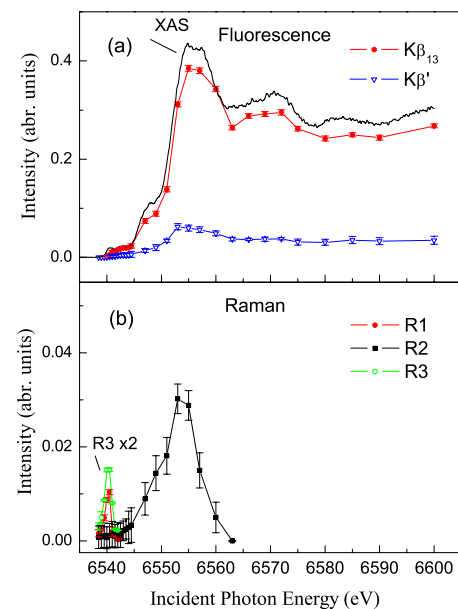

FIG. 5. (Color online) Incident photon energy (E_i) dependence of the intensity of (a) the fluorescence components F1 (Mn $K\beta_{1,3}$) and F4 (Mn $K\beta'$) and (b) the Raman components R1, R2, and R3 of Mn $1s3p$-RXES spectra obtained for $TbMnO_3$ crystals.
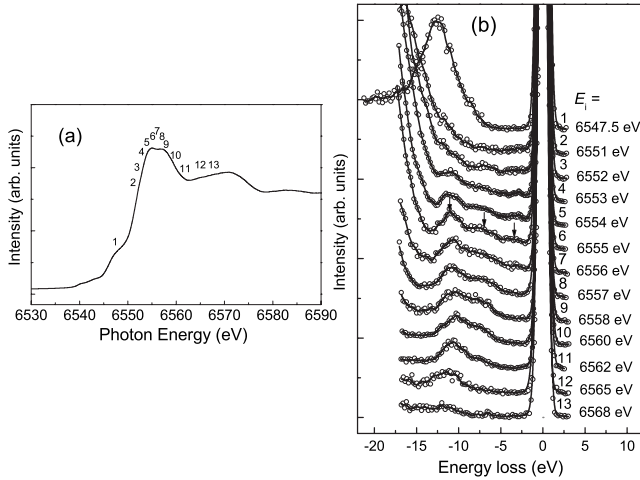
FIG. 6. (a) Mn K-edge x-ray absorption spectrum of TbMnO$_3$ crystals for $E\|c$ polarization measured with the total-fluorescence-yield mode. The number in the absorption spectrum indicates the incident photon energy used for RIXS measurement (b) Incident energy (E_i) dependence of RIXS intensity for TbMnO$_3$ as a function of energy loss at a fixed momentum transfer $Q=(0,0,6.95)$. Three prominent RIXS features at ~ 2.9, 7, and 11 eV are shown by arrows.

weak on-site Mn $1s$-$3d$ quadrupolar transition, on-site Mn $1s$-Mn $3d$ dipolar assisted transition, and off-site Mn $1s$-Mn$'$ $3d$ dipolar transition mediated by O $2p$ states.[54]

Figure 6(a) shows the Mn K-edge x-ray absorption spectrum of TbMnO$_3$ crystals for $E\|$c polarization measured in the total-fluorescence-yield mode. The number in the absorption spectrum indicates the incident photon energy used for the RIXS measurement. We measured RIXS spectra on varying the energy of the incident x-ray to determine the resonant energy. In Fig. 6(b), the incident energy (E_i) dependence of the RIXS intensity for TbMnO$_3$ as a function of energy loss (E_i-E_f) at a fixed momentum transfer $Q=(0,0,6.95)$ was reproduced. These data were recorded at room temperature. As shown in Fig. 6(b), at $E_i=6547.5$ eV, no feature is observed except a strong elastic scattering at zero energy transfer and broad scattering of the Mn $K\beta_{2,5}$ emission line ($3d \rightarrow 1s$). When the incident photon energy was tuned near the white line of the Mn K-edge spectrum (6553–6555 eV), the resonant enhancement of x-ray scattering is clearly observed, revealing three prominent RIXS features at ~ 2.9, 7, and 11 eV. The 7 and 11 eV peaks reach their respective maximum intensity at $E_i=6555$ eV, whereas the 2.9 eV peak reaches its maximum intensity at $E_i=6553$ eV.

To investigate the character of these resonant features, we measured the momentum dependence of the RIXS spectrum. Figures 7(a) and 7(b) show the Q dependence of RIXS spectra along the $Q(0,0,l)$ direction of TbMnO$_3$ crystals at incident photon energies 6555 eV and 6553 eV, respectively. The resonant feature at loss energy 11 eV shows a nearly flat dispersion. As noted from Figs. 7(a) and 7(b), the 2.9 eV band is broad, ranging from 2 to 4 eV, and shows a more or less dispersion relation. The relative RIXS intensity of these peaks varies with momentum. The intensities of the 2.9, 7, and 11 eV peaks generally increase as Q is increased.
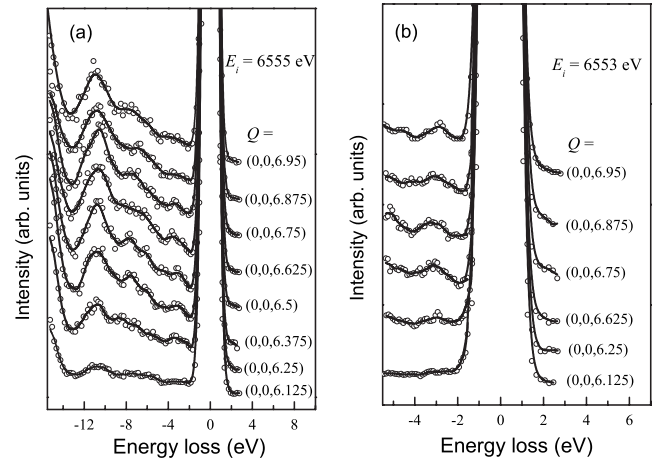

FIG. 7. Q dependence of RIXS spectra along the $Q(0,0,l)$ direction of TbMnO$_3$ crystals at incident photon energies of (a) 6555 eV and (b) 6553 eV.

To clarify the origin of these resonant features, we compare the RIXS result with the present *ab initio* calculations. On comparing the RIXS peak positions with the band diagram of TbMnO$_3$ based on the GGA+U calculations, the 7 eV region corresponds to transitions from O $2p$ states to unoccupied minority Mn $3d$ states, whereas the 11 eV band is ascribed to transitions from O $2p$ bands to empty Tb $5d$ bands. As shown in Fig. 1(c), the occupied $e_g^1\uparrow$ and unoccupied $e_g^2\uparrow$ bands of orthorhombic TbMnO$_3$ are predominated by $d_{3x^2-r^2}$ and $d_{y^2-z^2}$ orbitals, respectively, in one coplanar Mn(1) ion, whereas they exhibit primarily $d_{3y^2-r^2}$ and $d_{x^2-z^2}$ character, respectively, for the other coplanar Mn(2) ion. An intrasite d-d excitation, a transition from $d_{3y^2-r^2}$ to $d_{x^2-z^2}$ on the same Mn(2) atom, is symmetry forbidden, but a nonlocal intersite d-d excitation, in which a Mn(2) $3d_{3y^2-r^2}$ electron is excited from its neighboring empty Mn(1) $3d_{y^2-z^2}$ orbitals, is symmetry allowed. The intersite d-d orbital excitation between two nearest-neighbor transition-metal ions with singly occupied orthogonal e_g^1 orbitals of TbMnO$_3$ (two orthogonal e_g^1 orbitals are singly occupied in the intermediate excited states in a transition-metal site), i.e., Mn $3d_i^4(t_{2g}^3 e_g^1)$-Mn$'$ $3d_j^4(t_{2g}^3 e_g^1) \rightarrow$ Mn $3d_i^3(t_{2g}^3)$-Mn$'$ $3d_j^5(t_{2g}^3 e_g^2)$ excitations, corresponds to ferromagnetic superexchange interactions, predicted according to the Goodenough-Kanamori rule.[21,22,55] As evidenced in Figs. 3(b) and 5(b), the off-site dipole Mn $1s$-Mn$'$ $3d$ transitions make a considerable contribution to RXES processes.[53] The oxygen-mediated Mn $4p$-Mn$'$ $3d$ intersite hybridization creates low-lying empty states near the Fermi level that overlap in energy with Mn $3d$ empty states, as evidenced in RXES spectra in Fig. 3.[28,52,53,56] The broad 2.9 eV band is thus accounted for with coexisting on-site Mn $3d$-Mn $3d$ and off-site Mn $3d$-Mn$'$ $3d$ transitions. This explained why 2.9 eV band shows a relatively dispersion relation.

IV. CONCLUSION

For multiferroic TbMnO$_3$ crystals, we recorded resonant inelastic x-ray scattering at the Mn K edge and lifetime-

broadening-suppressed x-ray absorption spectra coupled with *ab initio* electron structure calculations to investigate 3*d* valence states and elementary electronic excitations. The polarized Mn *K*-edge x-ray absorption spectra show a strong polarization dependence, particularly for the white-line region, originating from a Jahn-Teller distortion and orbital ordering of MnO_6 octahedra in $TbMnO_3$. The 1*s*3*p*-RXES spectra of $TbMnO_3$ obtained at the Mn *K* edge reveal that the Raman regime is restricted predominantly to below the first pre-edge peak, whereas the fluorescence regime starts from the first pre-edge peak P1 of 1*s*→3*d* transitions, indicating a relatively delocalized character of unoccupied Mn 3*d* states. The additional Kβ emission profile at energy loss ~62 eV, observed at incident energies from pre-edge region to white line region, is attributed to the off-site dipole Mn 1*s*-Mn′ 3*d* and/or Mn 1*s*-Tb 5*d* transitions, as a consequence of hybridization of Mn 4*p* states with neighboring Mn′ 3*d*/Tb 5*d* orbitals. The off-site dipole Mn 1*s*-Mn′ 3*d* transitions make a considerable contribution to the pre-edge region of Mn *K*-edge spectrum. Three prominent RIXS features at ~2.9, 7, and 11 eV were observed. Based on GGA+*U* calculations, the 7 eV region corresponds to transitions from O 2*p* states to unoccupied minority Mn 3*d* states, whereas the 11 eV band is ascribed to transitions from O 2*p* bands to the empty Tb 5*d* band. The broad 2.9 eV band is accounted for with coexisting on-site Mn 3*d*-Mn 3*d* and off-site Mn 3*d*-Mn′ 3*d* transitions.

*Author to whom correspondence should be addressed. Electronic mail: jmchen@nsrrc.org.tw

[1] W. Luo, A. Franceschetti, M. Varela, J. Tao, S. J. Pennycook, and S. T. Pantelides, Phys. Rev. Lett. **99**, 036402 (2007).

[2] Y. Tokura and N. Nagaosa, Science **288**, 462 (2000).

[3] A. Tebano, C. Aruta, S. Sanna, P. G. Medaglia, G. Balestrino, A. A. Sidorenko, R. De Renzi, G. Ghiringhelli, L. Braicovich, V. Bisogni, and N. B. Brookes, Phys. Rev. Lett. **100**, 137401 (2008).

[4] M. Imada, A. Fujimori, and Y. Tokura, Rev. Mod. Phys. **70**, 1039 (1998).

[5] E. Dagotto, T. Hotta, and A. Moreo, Phys. Rep. **344**, 1 (2001).

[6] *Colossal Magnetoresistance Oxides*, edited by Y. Tokura (Gordon and Breach, New York, 2000).

[7] Y. Tokura, A. Urushibara, Y. Moritomo, T. Arima, A. Asamitsu, G. Kido, and N. Furukawa, J. Phys. Soc. Jpn. **63**, 3931 (1994).

[8] R. von Helmolt, J. Wecker, B. Holzapfel, L. Schultz, and K. Samwer, Phys. Rev. Lett. **71**, 2331 (1993).

[9] S. Jin, T. H. Tiefel, M. McCormack, R. A. Fastnacht, R. Ramesh, and L. H. Chen, Science **264**, 413 (1994).

[10] W. E. Pickett and D. J. Singh, Phys. Rev. B **53**, 1146 (1996).

[11] M. S. Laad, L. Craco, and E. Müller-Hartmann, New J. Phys. **6**, 157 (2004).

[12] T. Kimura, T. Goto, H. Shintani, K. Ishizaka, T. Arima, and Y. Tokura, Nature (London) **426**, 55 (2003).

[13] N. Hur, S. Park, P. A. Sharma, J. S. Ahn, S. Guha, and S. W. Cheong, Nature (London) **429**, 392 (2004).

[14] T. Goto, T. Kimura, G. Lawes, A. P. Ramirez, and Y. Tokura, Phys. Rev. Lett. **92**, 257201 (2004).

[15] N. A. Spaldin and M. Fiebig, Science **309**, 391 (2005).

[16] W. Eerenstein, N. D. Mathur, and J. F. Scott, Nature (London) **442**, 759 (2006).

[17] R. Ramesh and N. A. Spaldin, Nature Mater. **6**, 21 (2007).

[18] L. C. Chapon, G. R. Blake, M. J. Gutmann, S. Park, N. Hur, P. G. Radaelli, and S. W. Cheong, Phys. Rev. Lett. **93**, 177402 (2004).

[19] M. Fiebig, J. Phys. D **38**, R123 (2005).

[20] T. Kimura, G. Lawes, T. Goto, Y. Tokura, and A. P. Ramirez, Phys. Rev. B **71**, 224425 (2005).

[21] J. B. Goodenough, Phys. Rev. **100**, 564 (1955).

[22] J. J. Kanamori, Phys. Chem. Solids **10**, 87 (1959).

[23] R. M. White, *Quantum Theory of Magnetism* (Springer-Verlag, Berlin, 2007).

[24] P. A. Lee, N. Nagaosa, and X. G. Wen, Rev. Mod. Phys. **78**, 17 (2006).

[25] J.-S. Zhou and J. B. Goodenough, Phys. Rev. Lett. **96**, 247202 (2006).

[26] T. Kimura, S. Ishihara, H. Shintani, T. Arima, K. T. Takahashi, K. Ishizaka, and Y. Tokura, Phys. Rev. B **68**, 060403 (2003).

[27] J. Salafranca and L. Brey, Phys. Rev. B **73**, 024422 (2006).

[28] I. S. Elfimov, V. I. Anisimov, and G. A. Sawatzky, Phys. Rev. Lett. **82**, 4264 (1999).

[29] J. B. Goodenough, J. Appl. Phys. **81**, 5330 (1997).

[30] F. Bridges, C. H. Booth, M. Anderson, G. H. Kwei, J. J. Neumeier, J. Snyder, J. Mitchell, J. S. Gardner, and E. Brosha, Phys. Rev. B **63**, 214405 (2001).

[31] J. P. Rueff, L. Journel, P. E. Petit, and F. Farges, Phys. Rev. B **69**, 235107 (2004).

[32] J. B. Goodenough, *Magnetism and the Chemical Bond* (Wiley, New York, 1963).

[33] D. I. Khomskii and G. A. Sawatzky, Solid State Commun. **102**, 87 (1997).

[34] R. Kajimoto, H. Yoshizawa, H. Shintani, T. Kimura, and Y. Tokura, Phys. Rev. B **70**, 012401 (2004).

[35] T. Arima, T. Goto, Y. Yamasaki, S. Miyasaka, K. Ishii, M. Tsubota, T. Inami, Y. Murakami, and Y. Tokura, Phys. Rev. B **72**, 100102 (2005).

[36] N. Aliouane, D. N. Argyriou, J. Strempfer, I. Zegkinoglou, S. Landsgesell, and M. v. Zimmermann, Phys. Rev. B **73**, 020102(R) (2006).

[37] A. Kotani and S. Shin, Rev. Mod. Phys. **73**, 203 (2001).

[38] M. Z. Hasan, E. D. Isaacs, Z. X. Shen, L. L. Miller, K. Tsutsui, T. Tohyama, and S. Maekawa, Science **288**, 1811 (2000).

[39] S. Grenier, J. P. Hill, V. Kiryukhin, W. Ku, Y. J. Kim, K. J. Thomas, S. W. Cheong, Y. Tokura, Y. Tomioka, D. Casa, and T. Gog, Phys. Rev. Lett. **94**, 047203 (2005).

[40] T. Inami, T. Fukuda, J. Mizuki, S. Ishihara, H. Kondo, H. Nakao, T. Matsumura, K. Hirota, Y. Murakami, S. Maekawa, and Y. Endoh, Phys. Rev. B **67**, 045108 (2003).

[41] K. Ishii, K. Tsutsui, Y. Endoh, T. Tohyama, K. Kuzushita, T. Inami, K. Ohwada, S. Maekawa, T. Masui, S. Tajima, Y. Murakami, and J. Mizuki, Phys. Rev. Lett. **94**, 187002 (2005).

[42] E. Collart, A. Shukla, J. P. Rueff, P. Leininger, H. Ishii, I. Jarrige, Y. Q. Cai, S. W. Cheong, and G. Dhalenne, Phys. Rev. Lett. **96**, 157004 (2006).

[43] G. Kresse and D. Joubert, Phys. Rev. B **59**, 1758 (1999).

[44] A. I. Liechtenstein, V. I. Anisimov, and J. Zaanen, Phys. Rev. B **52**, R5467 (1995).

[45] S. Picozzi, K. Yamauchi, G. Bihlmayer, and S. Blügel, Phys. Rev. B **74**, 094402 (2006).

[46] I. Solovyev, N. Hamada, and K. Terakura, Phys. Rev. Lett. **76**, 4825 (1996).

[47] K. Yamauchi, F. Freimuth, S. Blugel, and S. Picozzi, Phys. Rev. B **78**, 014403 (2008).

[48] D. Senff, P. Link, K. Hradil, A. Hiess, L. P. Regnault, Y. Sidis, N. Aliouane, D. N. Argyriou, and M. Braden, Phys. Rev. Lett. **98**, 137206 (2007).

[49] Y. Joly, Phys. Rev. B **63**, 125120 (2001).

[50] H. Hayashi, Y. Udagawa, W. A. Caliebe, and C.-C. Kao, Phys. Rev. B **66**, 033105 (2002).

[51] H. Yamaoka, H. Oohashi, I. Jarrige, T. Terashima, Y. Zou, H. Mizota, S. Sakakura, T. Tochio, Y. Ito, E. Ya. Sherman, and A. Kotani, Phys. Rev. B **77**, 045135 (2008).

[52] A. Shukla, M. Calandra, M. Taguchi, A. Kotani, G. Vankó, and S. W. Cheong, Phys. Rev. Lett. **96**, 077006 (2006).

[53] F. de Groot, G. Vankó, and P. Glatzel, J. Phys.: Condens. Matter **21**, 104207 (2009).

[54] C. Gougoussis, M. Calandra, A. Seitsonen, Ch. Brouder, A. Shukla, and F. Mauri, Phys. Rev. B **79**, 045118 (2009).

[55] C. C. Chen, B. Moritz, F. Vernay, J. N. Hancock, S. Johnston, C. J. Jia, G. Chabot-Couture, M. Greven, I. Elfimov, G. A. Sawatzky, and T. P. Devereaux, arXiv:1002.4683v1 (unpublished).

[56] J. Joly, D. Cabaret, H. Renevier, and C. R. Natoli, Phys. Rev. Lett. **82**, 2398 (1999).